

Supporting Information

High-performance strain sensors using flexible micro-porous 3D-graphene with conductive network synergy

Jinqiu Zhang¹, Shanshui Lian¹, Fanghao Zhu¹, Gengqiang Cao¹, Hui Ma¹, Bingkun Wang¹, Huijuan Wu¹, Ziqi Zhao¹, Zhiduo Liu^{2,*} and Gang Wang^{1,3,*}

¹Department of Microelectronic Science and Engineering, School of Physical Science and Technology, Ningbo University, Ningbo 315211, P. R. China.

²Centre for Quantum Physics, Key Laboratory of Advanced Optoelectronic Quantum Architecture and Measurement (MOE), School of Physics, Beijing Institute of Technology, Beijing 100081, P. R. China.

³State Key Laboratory of Materials for Integrated Circuits, Shanghai Institute of Microsystem and Information Technology, Chinese Academy of Sciences, Shanghai 200050, P. R. China.

*Correspondence to: liuzhiduo@bit.edu.cn (Z. Liu); gangwang@nbu.edu.cn (G. Wang);

1. Height distribution before and after the transfer

The AFM morphology of 3D-graphene on the Si substrate and on the PDMS substrate after transfer was characterized, as shown in **Fig. S1**. No significant differences were observed in the morphology of the 3D-graphene before and after transfer (**Fig. S1(a-b)**), and the height remained consistent (**Fig. S1(c-d)**). This indicates that no noticeable damage occurred during the peeling process.

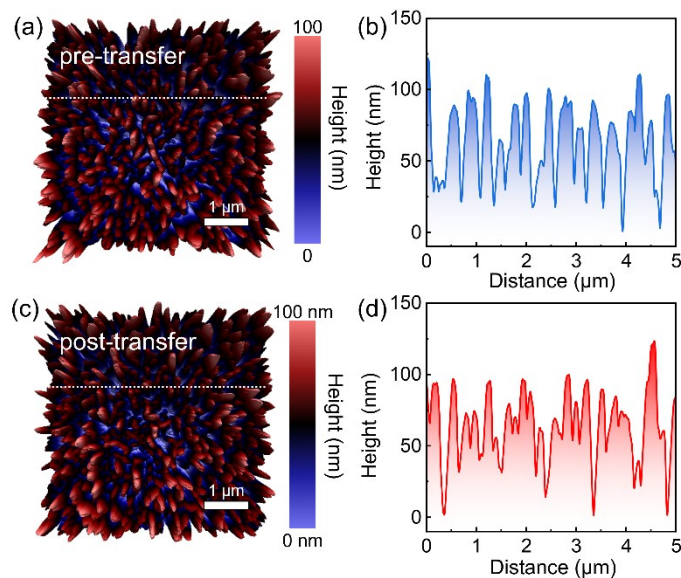


Fig. S1. (a) 3D topographic AFM image of the 3D-graphene on Si. (b) Height of 3D-graphene along the white dotted line shown in (a). (c) 3D topographic AFM image of the 3D-graphene on PDMS. (d) Height of 3D-graphene along the white dotted line shown in (a).

2. Porosity plot of the 3D-graphene.

The porous nature of the 3D-graphene is illustrated in **Fig. S2**, an estimated porosity of 70%. The high porosity of 3D-graphite provides a larger surface area and a multi-path conductive network, allowing the material to produce significant resistance changes even when subjected to small deformations. In addition, the porous structure helps to disperse the stresses and improve the fatigue resistance of the material, enabling it to maintain stable properties over multiple cyclic deformations.

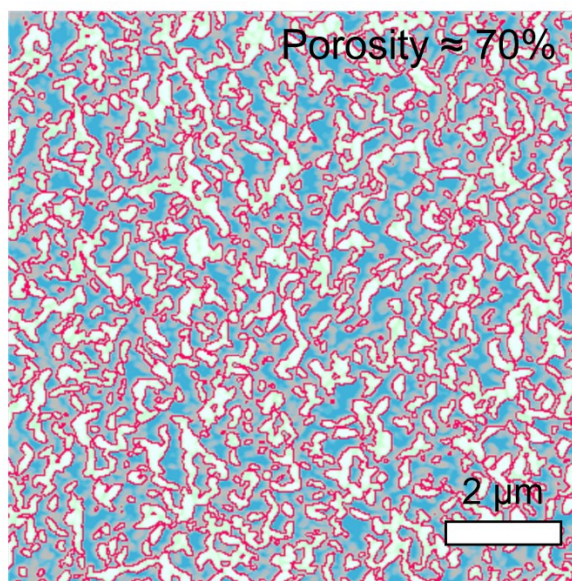


Fig. S2 Porosity plot of the 3D-graphene.

3. Thermal stability of three-dimensional graphene flexible strain sensors

The relative resistance changes of 3D-graphene flexible strain sensors under different temperature conditions at a fixed strain level of 11%, as shown in **Fig. S3**. The results demonstrate that the resistance variations of the 3D-graphene sensor remain within a controllable range, even as the temperature fluctuates. This observation highlights the sensor's remarkable ability to maintain high sensing stability when subjected to a thermal stress field. The exceptional performance of the 3D-graphene sensor can be attributed to the unique combination of its excellent mechanical properties and thermal conductivity. These properties enable the material to preserve its structural integrity and electrical characteristics under complex conditions involving coupled thermal and mechanical stresses. Specifically, the robust mechanical properties help the 3D-graphene film resist deformation-induced failures, while its high thermal conductivity facilitates rapid dissipation of localized heat, preventing the accumulation of thermal gradients that might otherwise compromise the sensor's performance. This synergistic interplay between the mechanical robustness and thermal management capabilities of 3D-graphene ensures that the sensor operates reliably across a wide range of environmental conditions.

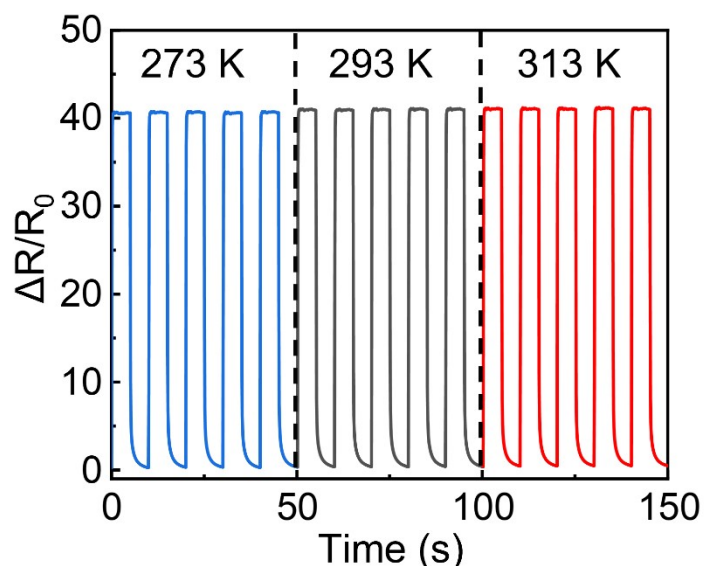


Fig. S3 Relative resistance changes of 3D-graphene flexible strain sensors stretched at different temperatures.

4. Variation of resistance and conductivity with strain

Fig. S4 illustrates the variation of resistance and conductivity with strain from 0% to 15%, and calculates the resistance (from 5×10^6 to $5 \times 10^7 \Omega$, **Fig. S4(a)**) and conductivity (from 5×10^{-7} to $2.5 \times 10^{-6} \text{ S}$, **Fig. S4(b)**) for different tensile strengths.

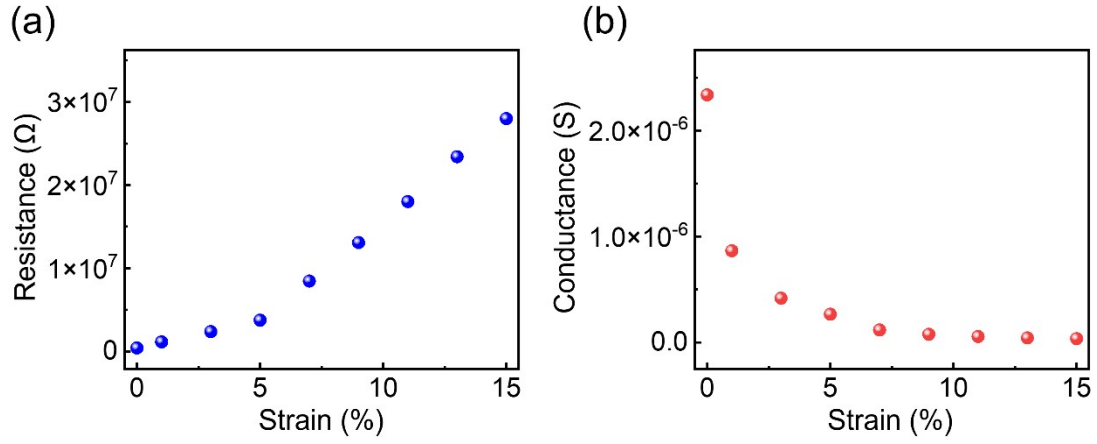


Fig. S4 (a) Strain-resistance curves in different strain ranges. (b) Strain-conductance curves in different strain ranges.

5. Mechanical stability and fatigue resistance of 3D-graphene flexible strain sensors

As shown in **Fig. S5(a)**, to verify the mechanical stability of the device, 1000 seconds continuous use test and 100 times tensile test were performed. The results show that the performance indexes of the sensor, such as sensitivity and response time, do not change much, indicating that it has good mechanical stability. In order to evaluate the fatigue resistance of the device, cyclic loading test was conducted, as shown in **Fig. S5(b)**. The test results showed that the sensor maintained a stable performance during repeated stretching without significant degradation or damage.

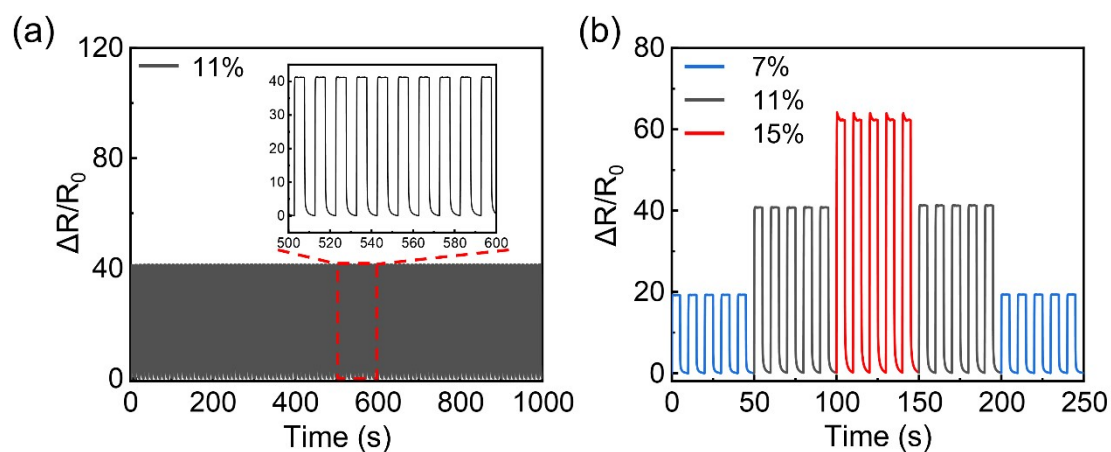


Fig. S5. (a) Real-time response of 11% stretch strain over 100 load-release cycles. (b) Strain cycling test with different tensile strength.

6. Summary of the performance of flexible strain sensors

Table S1 shows that the performance of some of the flexible strain sensors was compared, and as a result, most of the devices require large deformations to achieve high GF, while the 3D-graphene flexible strain sensors require only small deformations and anisotropic detection capabilities to achieve large GF.

Table S1. Performance comparison of flexible strain sensors.

Device structure	Strain (%)	GF _{//}	GF _⊥	Reference
MWCNTs@RGO	40	1888	—	1
MWCNT-MoS ₂	155	29.95	—	2
rGO/PDMS	300	44.01	—	3
CNTs films/PDMS	100	87	—	4
PVA/NaCl hydrogel	100	2.1	1.5	5
CCP	5	0.14	10.1	6
C ₅ A ₁₀ A _{1.5} -100 % hydrogel	300	3.45	1.61	7
CNTA/PDMS	10	2	30	8
AMNWAs	1	507	5	9
LCPT	100	630	0.2	10
3D-graphene/PDMS	15	413	22	Our work

References

1. Luo, W. Cao, K. Wu, H. Wang, X. Wang, H. Lin, K. Rui, Y. Yan and J. Zhu, *Chem. Eng. J.*, 2023, **465**, 142734.
2. M. N. Alam, V. Kumar, D. Lee and J. Choi, *Sensor Actuat. B-Chem*, 2023, 259, 110759.
3. X. Wang, Y. Tang, S. Cheng, Q. Gao, Y. Yuan, A. Li and S. Guan, *Compos. Part A-Appl S*, 2022, **161**, 107113.
4. S. Wang, P. Xiao, Y. Liang, J. Zhang, Y. Huang, S. Wu, S. Kuo and T. Chen, *J. Mater. Chem. C*, 2018, **6**, 5140-5147.
5. Q. Wang, Q. Zhang, G. Wang, Y. Wang, X. Ren and G. Gao, *ACS Appl. Mater. Interfaces*, 2022, **14**, 1921-1928.
6. H. Lin, W. Yuan, W. Zhang, R. Dai, T. Zhang, Y. Li, S. Ma and S. Song, *Carbohydr. Polym.*, 2025, **348**, 122781.
7. S. Chen, Y. Song, D. Ding, Z. Ling and F. Xu, *Adv. Funct. Mater.*, 2018, **28**, 1802547.
8. D. Li, H. Wang, Z. Han, Q. Wu, X. Lv, Y. Zhang, M. Wang, Z. Li and M. He, *Compos. Part B-Eng*, 2025, **291**, 112028.
9. M. Chen, P. Tang, R. Li, X. Li, X. Yi, H. Luan, X. Wang, C. Zhou, K. Zhou and J. Hu, *Chem. Eng. J.*, 2024, **496**, 153861.
10. C. Ma, M. Wang, K. Wang, P. C. Uzabakiriho, X. Chen and G. Zhao, *Adv. Fiber Mater.*, 2023, **5**, 1392-1403.